



Visible light-driven, selective CO₂ reduction in water by In-doped Mo₂C based on defect engineering

Shuaiqi Gong^a, Yanli Niu^a, Xue Teng^a, Xuan Liu^a, Mingze Xu^a, Chen Xu^a, Thomas J. Meyer^b, Zuofeng Chen^{a,*}

^a Shanghai Key Laboratory of Chemical Assessment and Sustainability, School of Chemical Science and Engineering, Tongji University, 1239 Siping Road, Shanghai 200092, China

^b Department of Chemistry, University of North Carolina at Chapel Hill, Chapel Hill, NC 27599, USA

ARTICLE INFO

Keywords:

Molybdenum carbide
Indium doping
Defects
CO₂ reduction
Photocatalysis

ABSTRACT

An In-doped Mo₂C (In@Mo₂C-d) is described as a photocatalyst for efficient and selective CO₂ reduction. It is prepared by a metal organic framework (MOF)-engaged approach combining ion exchange and carbothermal reduction and illustrates a self-core-shell nanoflower structure with rich defects. The photocatalyst performs visible light-driven CO₂-to-CO reduction with 97.3% selectivity at 234.4 μmol g⁻¹ h⁻¹ in aqueous media. Physicochemical measurements - isotopic labelling, time-resolved photoluminescence, *in situ* FT-IR, density functional theory - have been used to probe the photocatalytic mechanism. The combined analyses show that electrons are localized at neighboring Mo sites with localized defects and the d-band center is closer to the Fermi level after In doping, beneficial for the photocatalysis. They also suggest that In@Mo₂C-d can stabilize COOH* intermediates and facilitate CO* desorption. The results point to a previously unreported CO₂ reduction photocatalyst based on molybdenum carbide in which reactivity is promoted by doping and defect engineering.

1. Introduction

The atmospheric concentration of CO₂ continues to rise, increasing the importance of photocatalytic CO₂ reduction based on the carbon cycles [1–4]. Carbon monoxide (CO) is a useful intermediate in these cycles. It acts as a feedstock in the Fischer-Tropsch process which utilizes mixtures of CO and H₂ [5,6]. Photocatalysts have been developed for CO₂-to-CO conversion including metal oxides [7–10], metal sulfides [11,12], and semiconductor-based heterostructures [13–16], but their performances are limited in practical applications. Limitations arise from photocatalytic activation, poor product selectivity, and the use of non-aqueous environments. In designing photocatalytic systems, reduction of protons to H₂ in water is typically in competition with reduction of CO₂ which creates a significant challenge for CO₂ reduction. A goal in this area is the design of highly efficient photocatalysts in water with high stability and selectivity for CO₂ reduction.

Important factors in the design of transition metal catalysts for CO₂ reduction, include added surface metal sites that bind weakly to the C or O atoms of CO₂ by 2p-3d hybridization [17–19]. The M-C or M-O bonds are relatively weak, cleaving to form CO or hydrocarbon intermediates

[20]. In a recent plasma-assisted, catalytic CO₂ reduction study, molybdenum carbide was found to weaken the binding energy of adsorbed CO* due to enhanced carbophilic and oxophilic characters compared to metallic molybdenum [21]. It suggests that the free energy of CO* desorption may be lowered by carburizing transition metals for CO production. In another electrocatalytic study, with molybdenum carbide surfaces, adsorbed CO* was shown to undergo further hydrogenation to form CHO* leading to CH₄ production [22].

Despite these advances, to our knowledge, the use of transition-metal carbides as photocatalysts for efficient CO₂ reduction has not been explored. Theoretical studies suggest that CO₂ reduction to CO could be improved by stabilizing COOH* intermediates whose formation is usually the rate limiting step [23–25]. The binding energy for COOH* as an intermediate is suboptimal on monometallic surfaces, leading to the use of bimetallic catalysts [26–28], and catalysts with doped metal sites [24]. Doping is an effective route to implant extraneous elements into metal compounds [29–32]. It can create electronic states in the photocatalyst midgap region that can promote charge migration to the surface and provide local trap sites for photoexcited electrons on the surface for photocatalysis [33]. As an example, Liu *et al.* reported that the single

* Corresponding author.

E-mail address: zfchen@tongji.edu.cn (Z. Chen).

<https://doi.org/10.1016/j.apcatb.2022.121333>

Received 3 January 2022; Received in revised form 16 March 2022; Accepted 18 March 2022

Available online 21 March 2022

0926-3373/© 2022 Elsevier B.V. All rights reserved.

cobalt atom in $\text{Bi}_3\text{O}_4\text{Br}$ lowers the barrier for CO_2 activation. Addition of cobalt also stabilizes COOH^* intermediates and alters the rate-limiting step from forming COOH^* intermediates to CO^* desorption [24].

Recently, many studies focus on the photocatalysts with surface deficiency, in which the introduced defects serve as reactive centers to adsorb CO_2 molecules and subsequently activate them by lowering the adsorption energies [34–39]. To go further, the presence of abundant localized electrons in the defective sites can enhance the charge transfer between catalysts and adsorbates. Besides, the regulation of surface microstructure often demonstrates a significant effect on catalytic activity and selectivity of catalysts [40–43]. Accordingly, photocatalysts with appropriate dopants, rich defects, favorable microstructure and visible-light absorptivities are expected to serve as ideal structural models for boosting CO_2 photoreduction and for tailoring product selectivity.

We describe here a novel photocatalyst of atomic indium (In) doped molybdenum carbide (Mo_2C) for selective CO_2 reduction. Characterization of the target material ($\text{In@Mo}_2\text{C-d}$) reveals that incorporation of In in Mo_2C lattices induces rich defects which enable effective trapping of photoexcited electrons at surface catalytic sites. The photocatalyst performs visible light driven CO_2 -to- CO reduction by a selectivity of 97.3% at a rate of $234 \mu\text{mol g}^{-1} \text{h}^{-1}$ in aqueous media. Density functional theory (DFT) points to localized electron trapping at neighboring Mo sites with localized defects after In doping. Localization gives charge-enriched atomic sites that are activated for catalysis. Mechanistic studies also show that In doping lowers the CO_2 reduction barrier by stabilizing COOH^* intermediates with CO^* desorption rather than further reduction. The overall strategy, including an ion exchange doping, results in structural and compositional control of the photocatalyst. These results provide insights into the role of doping and defect engineering in promoting CO_2 photoreduction by the new molybdenum carbide-based photocatalyst.

2. Experimental

2.1. Experimental procedures

2.1.1. Synthesis of Mo-MOF nanoflowers

Typically, 0.41 g MoCl_5 and 1.32 g 2-methylimidazole were dissolved in 40 mL mixed solvents of methanol (20 mL) and ethanol (20 mL), respectively. Subsequently, the 2-methylimidazole solution was slowly dropped into the MoCl_5 solution under stirring. After 12 h, the orange precipitate was collected, cleaned with ethanol, and vacuum dried overnight.

2.1.2. Synthesis of In@Mo-MOF self-core-shell nanoflowers

The In@Mo-MOF self-core-shell nanoflowers were synthesized through an ion exchange method. Briefly, the collected orange Mo-MOF nanoflowers were dispersed in 40 mL mixed solution of methanol (20 mL) and ethanol (20 mL). Then, a certain amount of InCl_3 was dissolved in the suspension of Mo-MOF nanoflowers with stirring for 6 h. Finally, the dark orange powder was collected, followed by washing with ethanol and vacuum drying overnight. The amounts of InCl_3 added for synthesizing In@Mo-MOF-I, In@Mo-MOF-II, In@Mo-MOF-III and In@Mo-MOF-IV are 37, 75, 150, and 225 mg, respectively. Unless stated otherwise, In@Mo-MOF-II is abbreviated as In@Mo-MOF as the optimized sample in the paper.

2.1.3. Synthesis of In@Mo₂C-d

The obtained In@Mo-MOF was annealed in H_2/Ar (5%) at 600 °C for 3 h (heating rate, 3 °C/min).

2.1.4. Synthesis of Mo₂C-d

The obtained Mo-MOF was annealed in H_2/Ar (5%) at 600 °C for 3 h (heating rate, 3 °C/min).

2.1.5. Synthesis of In@Mo₂C

The obtained In@Mo-MOF was annealed in Ar at 600 °C for 3 h (heating rate, 3 °C/min).

2.1.6. Synthesis of Mo₂C

The obtained Mo-MOF was annealed in Ar at 600 °C for 3 h (heating rate, 3 °C/min).

2.2. Photocatalytic CO₂ reduction

2.2.1. CO₂ photoreduction measurements

The photocatalytic CO_2 reduction was performed in a gas-tight Pyrex cell reactor with an optical quartz window. In general, the catalyst (10 mg), distilled water (10 mL) and triethylamine (TEA, 2 mL) were added into the glass reaction vessel and dispersed ultrasonically. Subsequently, the reaction vessel was filled by CO_2 gas with a pressure around 80 kPa following complete evacuation. After the system is equilibrated, the reaction vessel was irradiated by a 300 W Xe lamp with 420 nm cutoff filter to allow merely the visible light passing ($\lambda > 420 \text{ nm}$). During the light irradiation upon the reaction vessel, the circulating cooling water was supplied to maintain the temperature. Generated gases were analyzed by gas chromatography at a time interval of 2 h.

2.2.2. Photoelectrochemical measurements

The photocatalyst (7 mg) was first ultrasonically dispersed in mixed solvents of ethanol (2 mL) and α -terpineol (1 mL). Next, ethyl cellulose (1 mg) was added into the suspension mixture and stirred overnight. The resulting ink was then coated onto a piece of F-doped SnO_2 (FTO) conducting glass. Lastly, the uniformly coated film electrode was available after drying in air.

Photoelectrochemical tests were performed with a three-electrode setup connected to an electrochemical workstation (CHI 760 A). The photocatalyst-coated FTO electrode was utilized as working electrode, Pt foil as counter electrode and Ag/AgCl as reference electrode with 0.5 M Na_2SO_4 as the electrolyte. The photocurrent curves were recorded with a 300 W Xe lamp (a 420 nm cutoff filter appended) at an on-and-off mode (time interval, 10 s). Electrochemical impedance spectroscopic (EIS) and linear sweep voltammetric (LSV) tests were conducted in 0.5 M KHCO_3 solution saturated with CO_2 . LSV curves were recorded at 10 mV/s.

2.2.3. AQE measurement for CO₂ photoreduction

The apparent quantum efficiency (AQE) for CO_2 reduction to CO was tested under a series of excitation wavelength irradiation with specific band-pass filters (300 W Xe lamp). The AQE for CO_2 to CO conversion can be determined as following:

$$\begin{aligned} \text{AQE (\%)} &= \frac{\text{numbers of the elections taking part in reduction}}{\text{numbers of incident photons}} \times 100\% \\ &= \frac{2n(\text{CO})}{I} \times 100\% \end{aligned}$$

where $n(\text{CO})$ means the amount of produced CO and I means the amount of incident photons.

3. Results and discussion

3.1. Preparation and characterization of defects-rich, In-doped Mo₂C

A synthetic procedure for the preparation of photocatalysts is illustrated in Fig. 1. It utilizes 2-methylimidazole and a Mo salt as the starting materials. Mo-based metal organic framework (Mo-MOF) nanoflowers are obtained by a precipitation reaction (Step I). They are doped with In to form In@Mo-MOF by ion exchange with InCl_3 used to give self-core-shell nanoflower structures (Step II). Defects-rich In@Mo₂C (In@Mo₂C-d) nanoflowers are obtained by a carbothermal

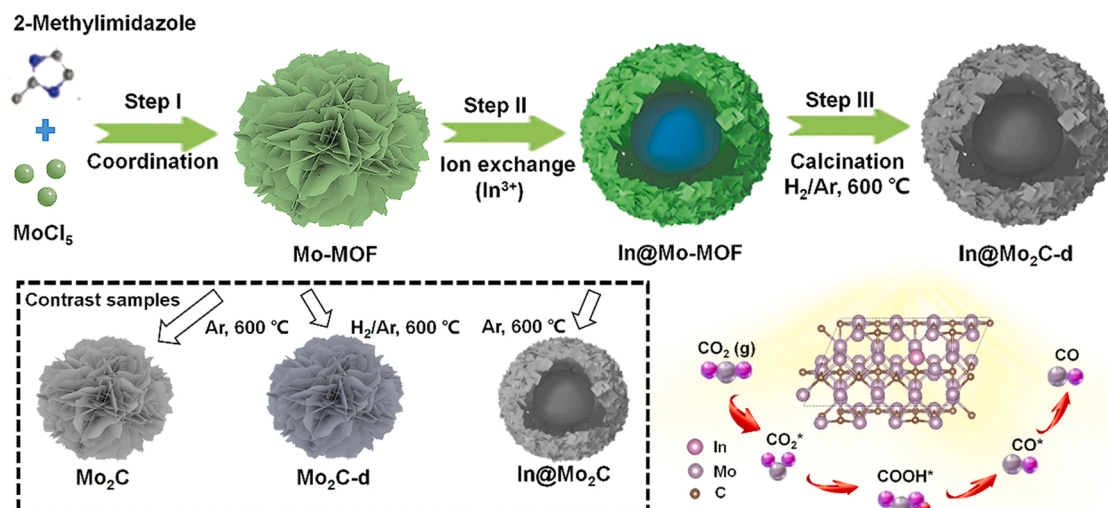


Fig. 1. Stepwise synthesis of self-core-shell In@Mo₂C-d nanoflowers (-d: defects-rich). The comparative samples Mo₂C, Mo₂C-d, and In@Mo₂C were prepared by varying the annealing atmosphere or by using undoped precursors.

reduction in a reductive H₂/Ar atmosphere (Step III). Comparative In@Mo₂C sample is prepared by annealing in Ar and, for Mo₂C-d and Mo₂C, in H₂/Ar and Ar atmospheres by using undoped Mo-MOF as a precursor. The roles of In doping and annealing conditions on material defects and consequently the photocatalytic performance are discussed below.

Scanning electron microscopic (SEM) images show a well-defined nanoflower structure for Mo-MOF (Fig. 2a). They are converted into self-core-shell nanoflowers of In@Mo-MOF by ion exchange, showing an apparent core-shell boundary (Fig. 2b). X-ray diffraction (XRD) pattern suggests that the crystalline structure of Mo-MOF is unchanged after In doping (Fig. S1). After annealing in a H₂/Ar atmosphere, the In@Mo₂C-d sample maintains the self-core-shell nanoflower morphology without significant changes (Fig. 2c). SEM images of contrast samples Mo₂C, Mo₂C-d, and In@Mo₂C are shown in Fig. S2 that confirm the effect of In doping on formation of core-shell morphology.

Transmission electron microscopy (TEM) elucidates different morphologies more clearly. A hollow structure with a distinct core and shell is observed for In@Mo₂C-d (Fig. 3a), while a solid structure is observed for the undoped materials (Fig. S3). In the high-resolution TEM (HRTEM) images of In@Mo₂C-d (Fig. 3b and S4), the lattice fringe in the core region has an average spacing of 0.265 nm assignable to the (100) plane of Mo₂C phase. A lattice fringe of 0.237 nm is identified at the outer edge due to the (101) plane of Mo₂C phase. The lattice spacings are increased compared to Mo₂C-d (0.26 nm for (100) and 0.23 nm for (101)) (Fig. S3), consistent with an In doping effect.

Energy-dispersive X-ray (EDX) elemental mappings for In@Mo₂C-d, reveal the presence of Mo, In, C, and N as elements with a uniform distribution throughout the sample (Fig. 3c). Intensity comparisons

show that the content of In as a dopant is much smaller compared to other elements. The levels of Mo and In are determined by inductively coupled plasma-optical emission spectrometry (ICP-OES). Analysis of working curves gives an atomic ratio of ~30:1 for the Mo:In ratio.

Addition of In, in the formation of self-core-shell structures, enhances the specific surface area. The Brunauer-Emmett-Teller (BET) surface area of In@Mo₂C is 42.327 m²/g, compared to Mo₂C at 27.147 m²/g (Fig. S5). The annealing atmosphere also affects the BET surface area [44–46]. In@Mo₂C-d obtained in H₂/Ar, with the appearance of additional material defects, has enhanced BET surface areas (56.735 m²/g) compared to In@Mo₂C in Ar (Fig. 3d).

XRD was used to determine the crystallinity of samples. As shown in Fig. 4a and S6, the β -Mo₂C phase appears in all samples with a hexagonal closest packing (HCP) crystal structure ($a = 3.012$ Å, $b = 3.012$ Å, $c = 4.735$ Å, space group P63/mm, JCPDS No. 35–0787). In doping in β -Mo₂C gives XRD peaks at 34.4 and 39.4° for the (100) and (101) planes of In@Mo₂C and In@Mo₂C-d. They are slightly shifted in the negative direction compared to that for the undoped carbides. The observation is consistent with the increase in lattice parameters a/b for β -Mo₂C after In doping in the lattice [47]. In the data, there is no diffraction peak for In consistent with the doping state of In.

Raman measurements provide additional insight. As shown in Fig. S7, Raman spectra for Mo₂C and Mo₂C-d include characteristic peaks at 663 and 820 cm⁻¹ for the Mo-C stretching mode in the Mo₂C phase. A band at 993 cm⁻¹ is consistent with a Mo=C bond in the β -Mo₂C phase [48,49]. Similar Raman spectra characteristics are observed for In@Mo₂C and In@Mo₂C-d with no evidence for In components. Although Raman spectra in the region of 100–1000 cm⁻¹ are complex, they are consistent with surface molybdenum oxides,

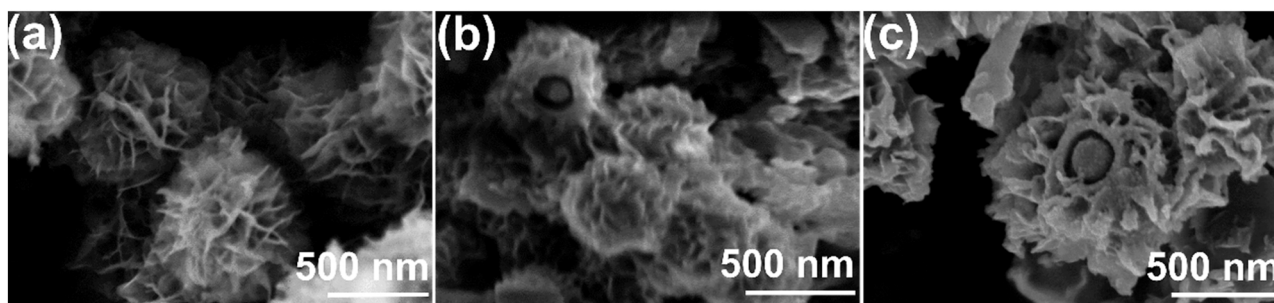


Fig. 2. SEM images of (a) Mo-MOF, (b) In@Mo-MOF, and (c) In@Mo₂C-d.

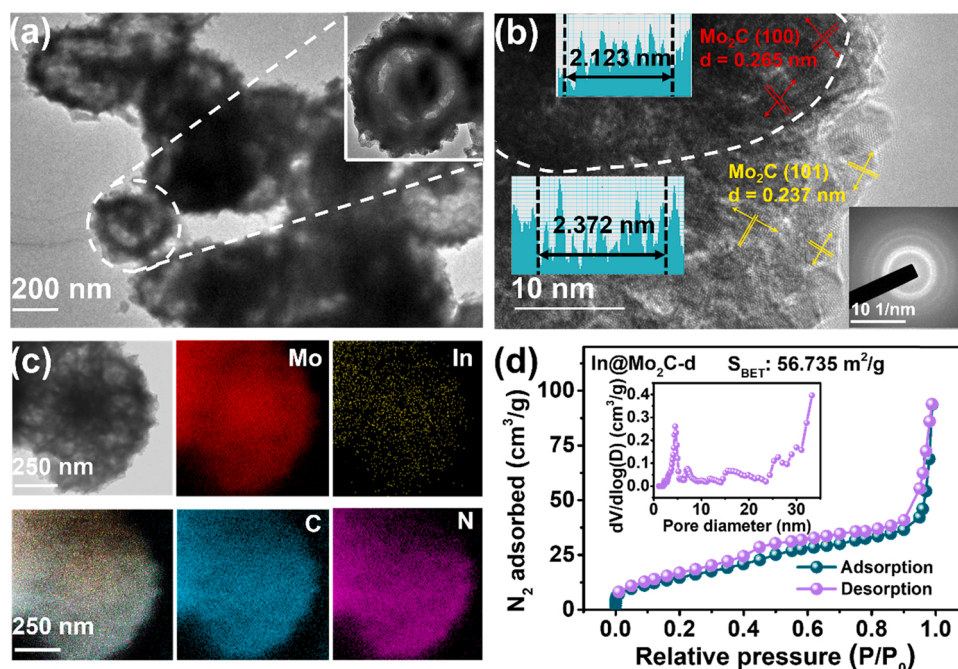


Fig. 3. (a) TEM images, (b) HRTEM image, (c) HAADF-STEM image and EDX elemental mapping images of In@Mo₂C-d. The inset image in (b) is the SAED pattern. (d) BET data for In@Mo₂C-d. The inset in (d) is a pore size distribution curve.

including MoO₃ and related oxides MoO_{3-x} from superficial oxidation. Note Fig. S8 for FT-IR data on the Mo-MOF precursor and resulting molybdenum carbides after annealing.

X-ray photoelectron spectroscopic (XPS) measurements on In@Mo₂C-d were used to explore its valence states and chemical composition (Fig. S9). The data show the existence of Mo, In, C, N and O. The existence of In is consistent with the doping of In into Mo₂C. For the high-resolution In 3d XPS spectrum in Fig. 4b, peaks at 445.0 and 452.5 eV arise from characteristic In³⁺ 3d_{5/2} and 3d_{3/2}. Fig. 4c displays Mo 3d XPS spectra for In@Mo₂C-d and Mo₂C-d showing deconvoluted peaks from Mo²⁺, Mo⁴⁺, and Mo⁶⁺ on the surfaces of the carbides. In contrast to Mo₂C-d (228.3 and 231.5 eV), bands for Mo²⁺ at 228.1 eV (Mo²⁺ 3d_{5/2}) and 231.2 eV (Mo²⁺ 3d_{3/2}) for Mo-C in In@Mo₂C-d shift negatively by ~0.2–0.3 eV. The shifts in binding energies are consistent with electronic interactions between Mo₂C and In induced by internal electron transfer. For C 1s XPS bands in Fig. 4d, the dominant features at 284.1 and 284.6 eV in In@Mo₂C-d arise from Mo-C and C-C bonds that are the primary chemical components in carbide materials.

Electron paramagnetic resonance (EPR) technique was applied to investigate the defects which serve as photogenerated electron trap sites in the photocatalysts. A resonance with a g-factor value of 2.003 is the observed characteristic of delocalized/free electrons arising from defects in the solid. As shown in Fig. 4e, its intensity follows the sequence, In@Mo₂C-d > In@Mo₂C > Mo₂C, suggesting that the doping of In and treatment in a reductive H₂/Ar atmosphere are both beneficial for creating defects. The defects-rich In@Mo₂C-d has improved photocatalytic performance.

3.2. Photocatalytic CO₂ reduction

CO₂ reduction was explored in deionized (DI) water under a 300 W Xe lamp with a 420 nm cutoff filter. TEA was added as a sacrificial agent. With visible light irradiation, Mo₂C produces CO at a rate of 56.4 μmol g⁻¹ h⁻¹ accompanied by CH₄ generation at 18.5 μmol g⁻¹ h⁻¹ (Fig. 5a-b). After In doping, CO production at In@Mo₂C is increased to 93.8 μmol g⁻¹ h⁻¹, a level 1.66 above pure Mo₂C. Controlled incorporation of defects in a H₂/Ar atmosphere gives In@Mo₂C-d, and increases the rate of CO reduction to 234.4 μmol g⁻¹ h⁻¹, around 2.50 and 4.15 times

higher than that for In@Mo₂C and Mo₂C, respectively. The increase in CO yield is accompanied by a decrease in the yield of CH₄ which enables a selectivity in In@Mo₂C-d toward CO₂ reduction. Because of the significant role of In doping on photocatalytic performance, the amount of added In in In@Mo₂C-d is optimized (Fig. S10). The photocatalytic CO₂ reduction performances of In@Mo₂C-d and other Mo-based catalysts are compared in Table S1. It is apparent that In@Mo₂C-d exhibits superior photocatalytic performance over other Mo-based catalysts.

The apparent quantum yields (AQE) for In@Mo₂C-d are 11.2% at 450 ± 20 nm and 7.2% at 550 ± 20 nm, respectively (Fig. 5c). Sequential cycling gives insight into the photocatalytic stability of the photocatalysts. A 4-cycle test, with a 40-h irradiation period, results in negligible loss of photocatalytic activity for CO production (Fig. 5d). The XRD pattern and SEM image of In@Mo₂C-d after a 40-h irradiation are shown in Fig. S11–12. The photocatalysis occurs with negligible changes in both structure and morphology.

Photocatalysis was extended to more broadly spectral irradiation. Irradiation with a 300 W Xe lamp, without a cutoff filter, results in CO production with a rate of 2055.5 μmol g⁻¹ h⁻¹ at In@Mo₂C-d (Fig. S13). On the other hand, irradiation by the near-infrared light with an appended 800 nm cutoff filter results in insignificant photocatalytic CO₂ reduction. Moreover, control experiments demonstrate that there is no detectable CO generation in the dark, in the absence of CO₂ or without photocatalyst (Fig. S14). The observations verify that CO is produced from CO₂ reduction over photocatalyst, driven by light irradiation. The gas chromatography-mass spectrometry (GC-MS) measurement was performed using ¹³CO₂ as the feedstock. A major signal at m/z = 29 (¹³CO) is observed, affirming further the origin of detected CO (Fig. 5e).

In a series of experiments, the roles of In doping and defect engineering were explored systematically. Based on UV-vis diffuse reflectance spectroscopy (DRS), In@Mo₂C-d has an enhanced visible light response beneficial for solar energy conversion (Fig. 6a). Chopped visible light irradiation reveals a remarkably enhanced photocurrent response at In@Mo₂C-d compared to Mo₂C, Mo₂C-d and In@Mo₂C (Fig. 6b). The comparison points to an important role for rapid separation and transportation of photogenerated charge carriers in In@Mo₂C-d.

Electrochemical impedance spectroscopy (EIS) reveals that

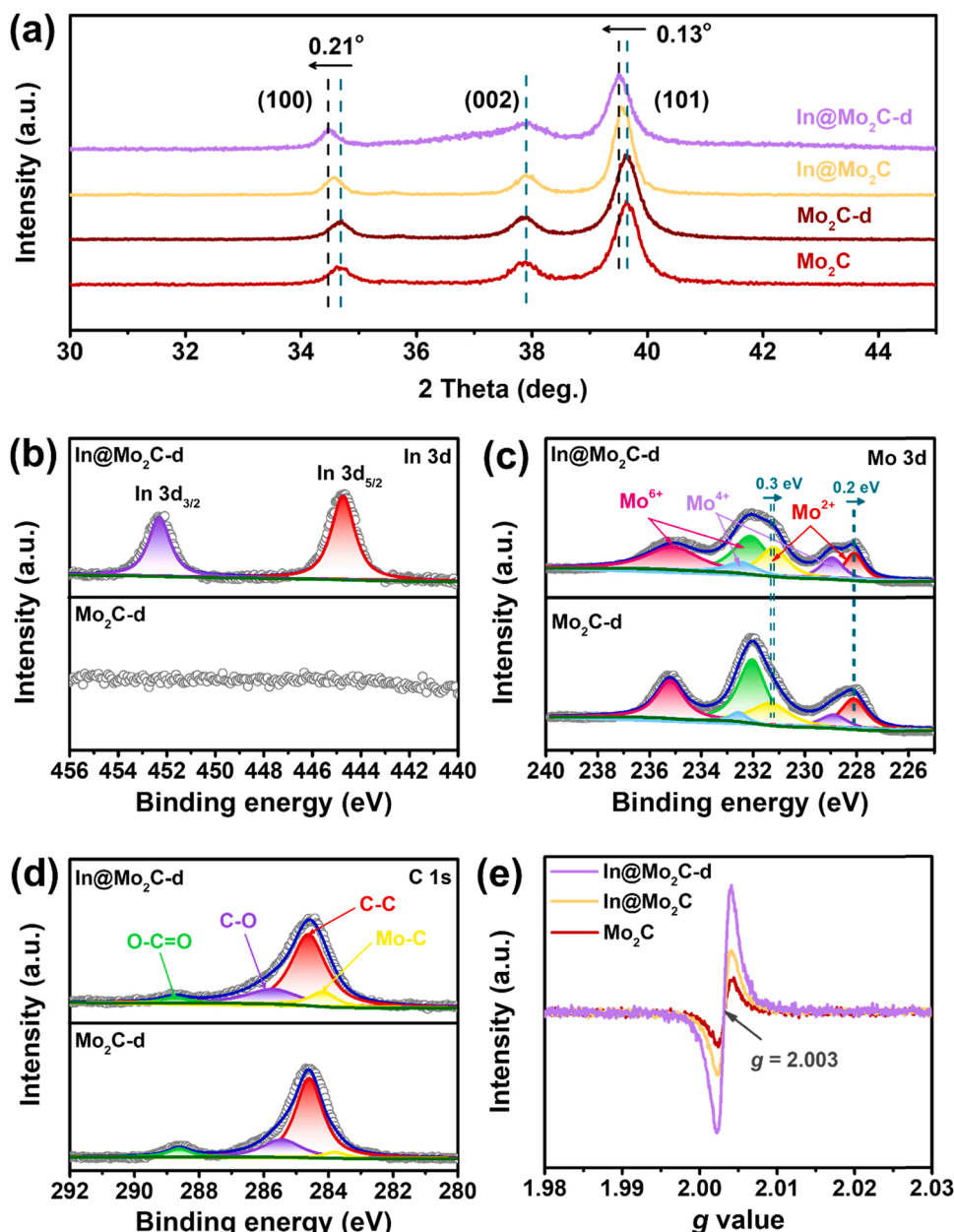


Fig. 4. (a) XRD patterns of Mo₂C, Mo₂C-d, In@Mo₂C, and In@Mo₂C-d. High-resolution XPS spectra of (b) In 3d, (c) Mo 3d and (d) C 1s of Mo₂C-d and In@Mo₂C-d. (e) EPR spectra of Mo₂C, In@Mo₂C and In@Mo₂C-d.

In@Mo₂C-d exhibits a minimum charge transfer resistance in Nyquist plots, enabling rapid separation and transportation of photogenerated electron-hole pairs (Fig. 6c). From linear sweep voltammograms (LSV), In@Mo₂C-d exhibits the largest current density among various samples (Fig. 6d). The same electrode undergoes different LSV performances under N₂, CO₂, or in the dark (Fig. S15). The combination of experiments show that In@Mo₂C-d can facilitate charge separation and transportation and promote highly efficient photocatalytic CO₂ reduction.

Photoluminescence (PL) measurements were also used to investigate the roles of In doping and defect formation (Fig. 7a). Compared to Mo₂C, the decrease in emission at 554 nm for Mo₂C-d is consistent with more efficient electron-hole separation caused by defects as trap sites. After In doping in Mo₂C, both In@Mo₂C and In@Mo₂C-d, exhibit red-shifted emissions at ~570 nm. Their emissions are strongly quenched and nearly vanished compared to undoped materials. It indicates forcefully suppressed recombination for photogenerated electron-hole pairs after In doping.

Charge carrier dynamics for Mo₂C, Mo₂C-d, In@Mo₂C, and In@Mo₂C-d were investigated by time-resolved photoluminescence spectroscopy (TRPL). The data (Fig. 7b and Table S2) show that formation of new defect levels enhances the average emission lifetime from 78.96 ns for Mo₂C to 97.11 ns for Mo₂C-d. Upon In doping, the emission lifetime is further prolonged to 133.08 ns at In@Mo₂C-d through trapping photoexcited electrons. Together, efficient separation and inhibited recombination of interfacial charge carriers lead to enhanced photocatalytic CO₂ reduction in defects-rich In@Mo₂C-d.

3.3. Mechanisms for photocatalytic CO₂ reduction

The In doping is verified by increased (100) and (101) lattice spacings in In@Mo₂C-d and the negatively-shifted diffraction peaks for these planes. Meanwhile, the EPR spectroscopy reveals rich defects for In@Mo₂C-d. For transition metal carbides, defects are usually associated with carbon vacancies, especially by implanting extraneous elements as

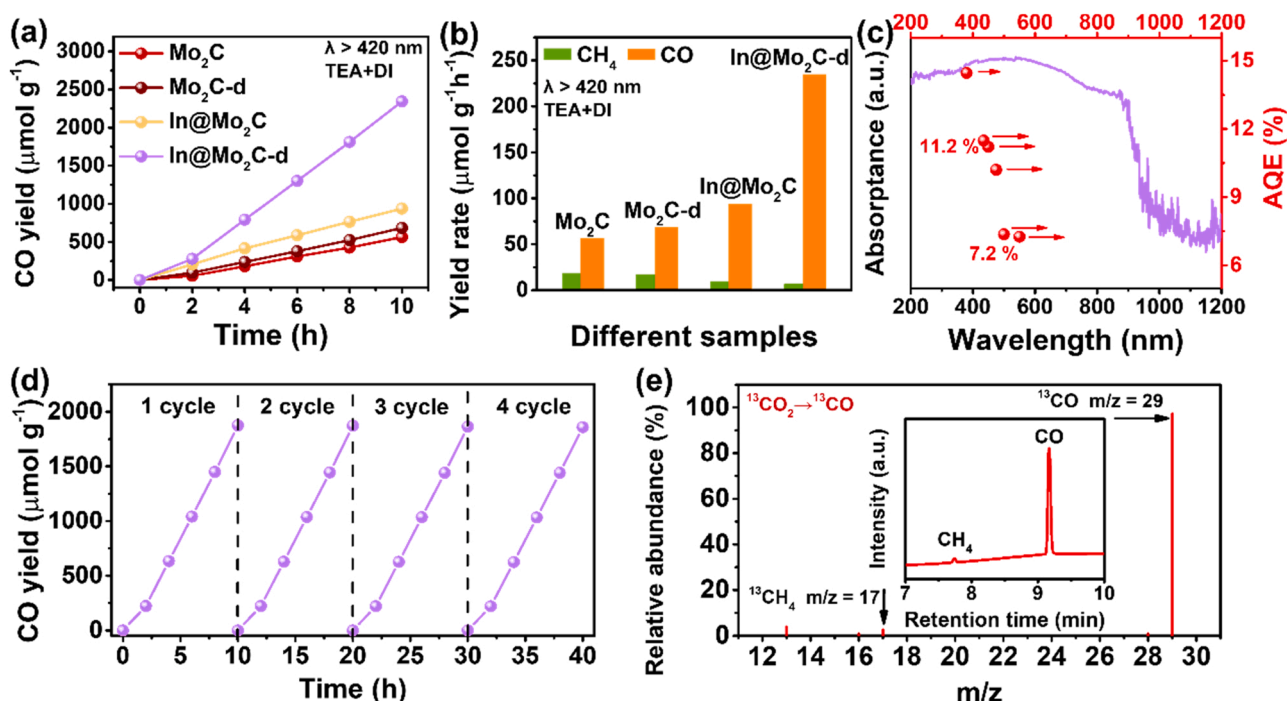


Fig. 5. (a) CO production and (b) average gas evolution rates for CH_4 and CO in aqueous solutions over a series of photocatalysts under visible light irradiation for 10 h. (c) The CO AQE for $\text{In@Mo}_2\text{C-d}$. (d) Continuously cycled production of CO at $\text{In@Mo}_2\text{C-d}$ under visible light irradiation. (e) Mass spectrum for ^{13}CO yielded on $\text{In@Mo}_2\text{C-d}$ with $^{13}\text{CO}_2$. The inset is the GC spectrum.

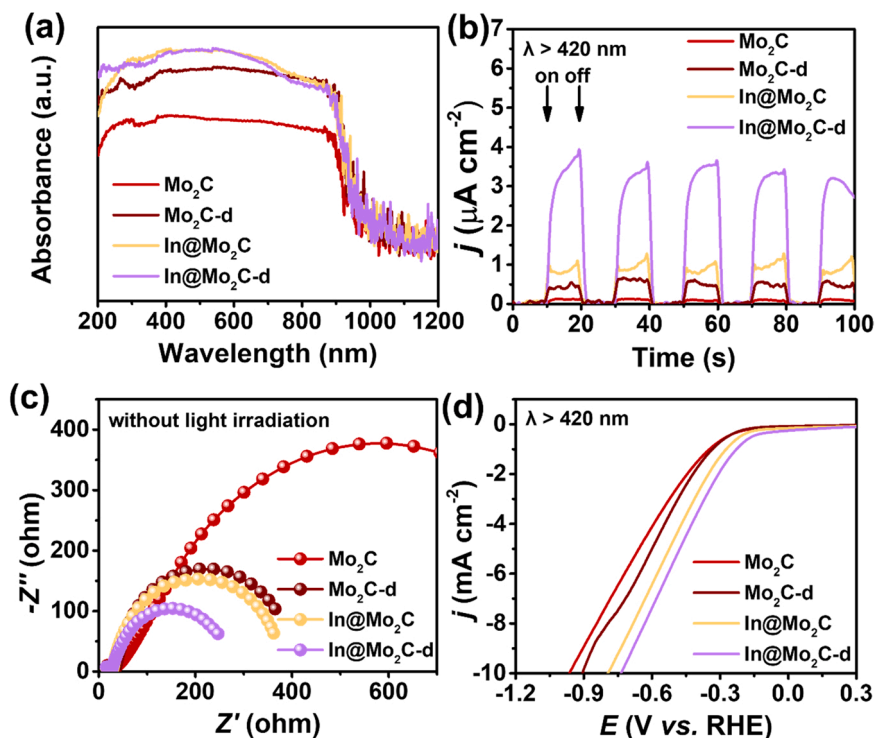


Fig. 6. (a) UV-vis DRS of Mo_2C , $\text{Mo}_2\text{C-d}$, $\text{In@Mo}_2\text{C}$ and $\text{In@Mo}_2\text{C-d}$. (b) Photocurrent response of Mo_2C , $\text{Mo}_2\text{C-d}$, $\text{In@Mo}_2\text{C}$ and $\text{In@Mo}_2\text{C-d}$ upon chopped visible light irradiation. (c) EIS of Mo_2C , $\text{Mo}_2\text{C-d}$, $\text{In@Mo}_2\text{C}$ and $\text{In@Mo}_2\text{C-d}$ in CO_2 -saturated 0.5 M KHCO_3 with no irradiation. (d) LSV curves of Mo_2C , $\text{Mo}_2\text{C-d}$, $\text{In@Mo}_2\text{C}$ and $\text{In@Mo}_2\text{C-d}$ in CO_2 -saturated 0.5 M KHCO_3 under visible light irradiation.

dopants [50]. The appearance of In doping, with abundant defects, may enable CO_2 adsorption/activation with three possible structures for In doping (Fig. S16). To model possible carbon vacancies in the In-doped Mo_2C (100) surface, the formation energies for carbon vacancies were

calculated (Fig. S17). On comprehensive consideration, the relatively stable structure with low formation energy and more carbon vacancies is chosen as the theoretical model.

DFT calculations were utilized to unravel the influence of In-doping

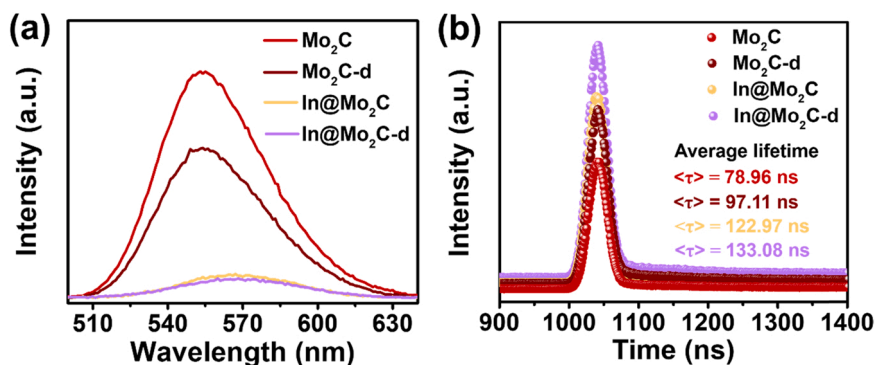


Fig. 7. (a) Steady-state PL spectra and (b) time-resolved PL spectra for Mo₂C, Mo₂C-d, In@Mo₂C and In@Mo₂C-d.

and localized defects on electronic structure. Based on the calculated density of states (DOS) (Fig. 8a), In doping creates a new dopant level near the Fermi energy (E_f) as potential reduction site. Additionally, the presence of defects results in the appearance of a new defect level in In@Mo₂C-d as evidenced by the change of C orbit. The DOS near the E_f , which mainly originates from the d state, was further investigated to probe the electronic interaction (Fig. 8b). The d-bands of transition metals are associated with adsorption and catalytic activities, because the coupling between d-band states in metals and valence states of adsorbates induces electronic interactions (e.g., adsorption and binding) [51]. A d-band center close to E_f makes it easier for electrons to escape and triggers catalytic reactions. The d-band centers of Mo₂C, In@Mo₂C and In@Mo₂C-d relative to E_f are calculated to be -1.33 eV, -1.10 eV and -0.91 eV, respectively. The d-band center shifts obviously toward E_f after In doping and the upshift of the d-band center is beneficial for the overall catalytic reaction. In addition, the charge density differences for In@Mo₂C (Fig. 8c) and In@Mo₂C-d (Fig. 8d) clearly points to localized electron trapping at neighboring Mo sites with localized defects. It suggests that In atoms can alter the electronic structure of Mo₂C, making Mo electron-rich to promote CO₂ reduction. The electrons in the defect structure, the usual catalytically active sites, are more likely to be activated.

To dive deep into the interfacial photocatalysis, CO₂ adsorption, activation, and CO desorption were probed. As the initial step, CO₂ adsorption plays a crucial role in CO₂ reduction process. Fig. 9a shows CO₂ adsorption isotherms of Mo₂C, In@Mo₂C and In@Mo₂C-d. The data

indicate that both In doping and defects engineering can enhance the CO₂ adsorption capacity. The formation of COOH* intermediates is usually regarded as the key step for CO₂ reduction to CO [24,52]. To probe the chemical activation of CO₂ molecules, *in situ* FT-IR measurement was performed on In@Mo₂C-d and Mo₂C-d under the gas-solid condition with a drop of CO₂-saturated solution. As shown in Fig. 9b, the peaks for CO₂*⁻ at 1265 cm⁻¹, bidentate (b-CO₃²⁻) at 1377 cm⁻¹, and HCO₃⁻ at 1442 cm⁻¹ are identified on In@Mo₂C-d before irradiation. Under light irradiation, the peak of the critical intermediate COOH* (1566 cm⁻¹) associated with CO production appears, which is gradually increased along with the irradiation time. The peaks of *OCH₃ at 1294 cm⁻¹ and *OCH₂ at 1348 cm⁻¹ for CH₄ production are insignificant on In@Mo₂C-d. By contrast, these peaks are relatively pronounced on Mo₂C-d (Fig. S18). These observations are consistent with their different product selectivity. CO desorption is also a significant step to photocatalytic CO₂ reduction. As seen from CO temperature programmed desorption (TPD) curves in Fig. 9c, In@Mo₂C-d exhibits the lowest onset desorption temperature. It suggests that produced CO* molecules may release more easily from In@Mo₂C-d than other samples.

To further explore the role of In doping, Gibbs free energy calculations were performed on In@Mo₂C-d and Mo₂C-d (Fig. 10a and S19-S20). According to calculated results, formation of COOH* intermediates is the rate limiting step for both samples, and In@Mo₂C-d has a much lower energy barrier (0.64 eV) than Mo₂C-d (1.50 eV) (Fig. 10b-c). This may be ascribed to the charge enrichment induced by In dopant

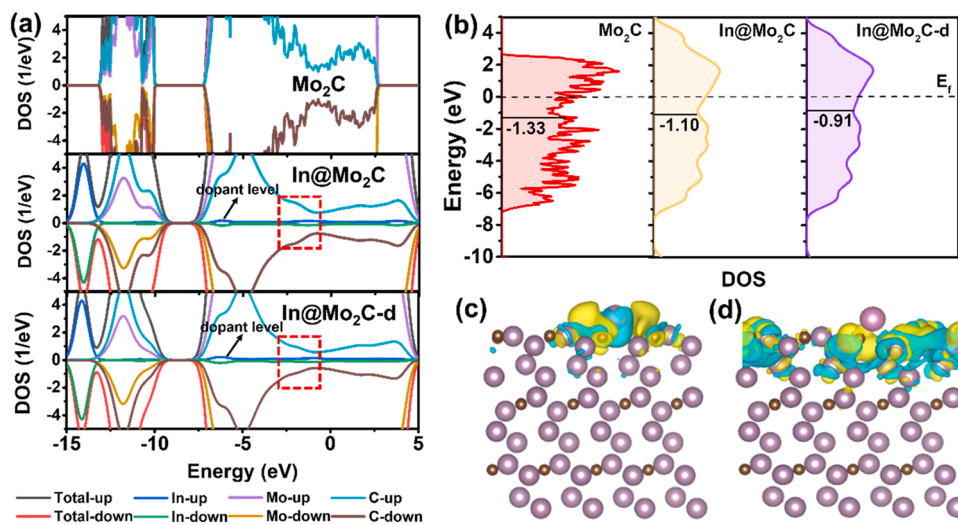


Fig. 8. (a) Calculated density of states (DOS) of Mo₂C, In@Mo₂C and In@Mo₂C-d. (b) Total density of states (TDOS) and d-band centers (black line) of Mo₂C, In@Mo₂C and In@Mo₂C-d. Crystal structure of In@Mo₂C (c) and In@Mo₂C-d (d) with differential charge densities (the yellow/blue area represents enrichment/loss of the charge).

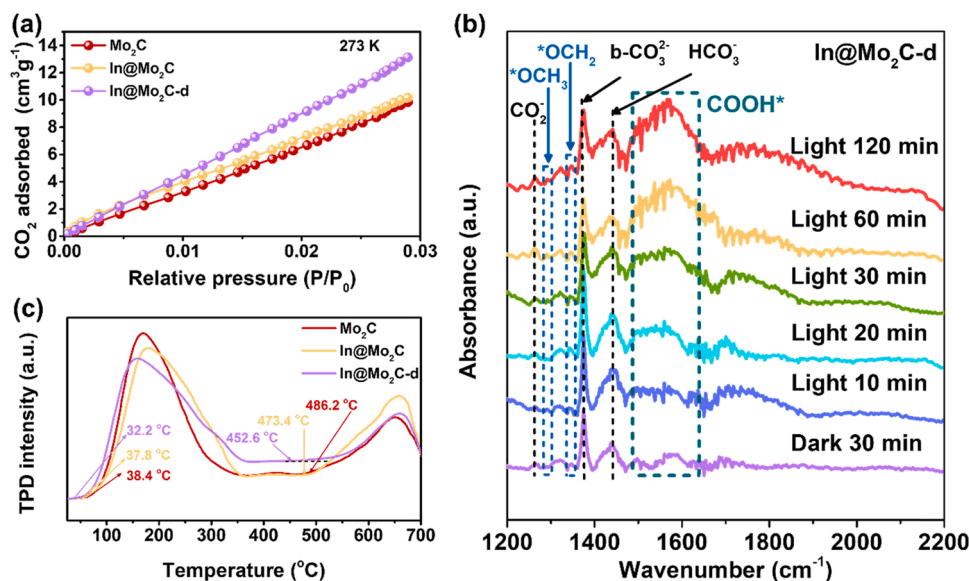


Fig. 9. (a) CO₂ adsorption isotherms of Mo₂C, In@Mo₂C and In@Mo₂C-d. (b) *In-situ* FT-IR spectra of In@Mo₂C-d during CO₂ reduction. (c) CO TPD curves of Mo₂C, In@Mo₂C and In@Mo₂C-d.

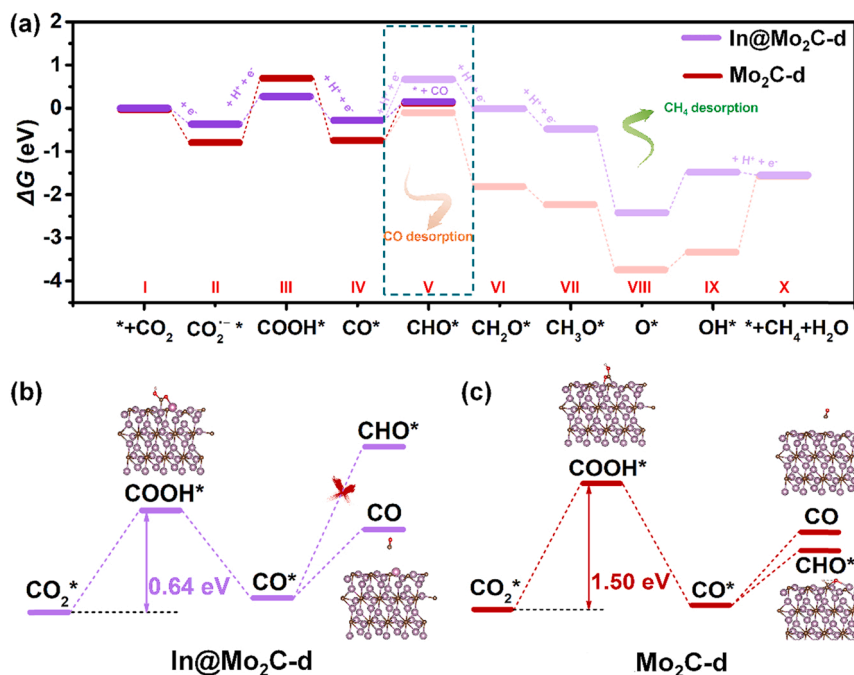


Fig. 10. Gibbs free energy calculations. (a) Free energy diagrams of photocatalytic CO₂ reduction to CO or CH₄ at In@Mo₂C-d and Mo₂C-d. Steps marked by the dashed box are crucial to determine the product selectivity. Key steps of photocatalytic CO₂ reduction to CO on In@Mo₂C-d (b) and Mo₂C-d (c).

and localized defects, note Fig. 8c-d above. The charge-enriched active sites can effectively stabilize the rate-limiting COOH* intermediates.

As revealed by step V (dashed box) in Fig. 10a, the desorption energy of CO molecules (ΔG (* + CO)) is apparently smaller than the hydrogenation energy for CHO* formation (ΔG (CHO*)). It implies that In@Mo₂C-d is favorable for liberation of CO* molecules from its surface as final product, rather than further reduction to generate CHO*. For Mo₂C-d, the desorption energy of CO* is slightly higher than that for hydrogenation. As a result, CO* molecules have a tendency to react with proton-electron pairs to produce CH₄, which is consistent with the relatively high amount of CH₄ produced on Mo₂C-d.

4. Conclusions

In summary, defects-rich, In-doping Mo₂C with a self-core-shell nanoflower structure have been prepared by a MOF-engaged strategy involving an ion exchange reaction and a carbothermal reduction reaction. Under visible light irradiation, In@Mo₂C-d can perform CO₂-to-CO reduction at a rate of 234.4 μmol g⁻¹ h⁻¹ with a selectivity of 97.3% in aqueous media. The (photo)electrochemical and photoluminescence characterizations verify efficient electron-hole separation/transport and suppressed charge recombination. The charge density difference indicates that electrons are localized at neighboring Mo sites with localized defects and the d-band center of In@Mo₂C-d is closer to the E_f after In doping, beneficial for the overall catalytic reaction. In photocatalysis,

In@Mo₂C-d can enhance CO₂ adsorption, boost CO₂ reduction to CO via stabilizing COOH* intermediates and facilitate CO* desorption. This study develops a new transition metal carbide photocatalyst for high-performance CO₂ reduction in water promoted by doping and defects engineering.

CRediT authorship contribution statement

S. Gong designed this study, conducted the experiments and wrote the paper; **Y. Niu**, **X. Teng**, **X. Liu**, **M. Xu**, and **C. Xu** did some characterizations and performed some data analyses; **T. J. Meyer** revised the paper; **Z. Chen** designed this study, performed some data analyses and revised the paper. All authors contributed to the general discussion.

Declaration of Competing Interest

The authors declare that they have no known competing financial interests or personal relationships that could have appeared to influence the work reported in this paper.

Acknowledgments

This work was supported by the National Natural Science Foundation of China (22072107, 21872105) and the Science & Technology Commission of Shanghai Municipality (19DZ2271500).

Appendix A. Supporting information

Supplementary data associated with this article can be found in the online version at [doi:10.1016/j.apcatb.2022.121333](https://doi.org/10.1016/j.apcatb.2022.121333).

References

- [1] C. Rice, J. Wolf, D.H. Fleisher, S.M. Acosta, S.W. Adkins, A.A. Bajwa, L.H. Ziska, Recent CO₂ levels promote increased production of the toxin parthenin in an invasive *Parthenium hysterophorus* biotype, *Nat. Plants* 7 (2021) 725–729.
- [2] W. Wang, S. Wang, X. Ma, J. Gong, Recent advances in catalytic hydrogenation of carbon dioxide, *Chem. Soc. Rev.* 40 (2011) 3703–3727.
- [3] J. Ran, M. Jaroniec, S.Z. Qiao, Cocatalysts in semiconductor-based photocatalytic CO₂ reduction: achievements, challenges, and opportunities, *Adv. Mater.* 30 (2018), 1704649.
- [4] C. Hepburn, E. Adlen, J. Beddington, E.A. Carter, S. Fuss, N. Mac Dowell, J.C. Minx, P. Smith, C.K. Williams, The technological and economic prospects for CO₂ utilization and removal, *Nature* 575 (2019) 87–97.
- [5] Z. Jiang, X. Xu, Y. Ma, H.S. Cho, D. Ding, C. Wang, J. Wu, P. Oleynikov, M. Jia, J. Cheng, Y. Zhou, O. Terasaki, T. Peng, L. Zan, H. Deng, Filling metal-organic framework mesopores with TiO₂ for CO₂ photoreduction, *Nature* 586 (2020) 549–554.
- [6] S. Gong, M. Hou, Y. Niu, X. Teng, X. Liu, M. Xu, C. Xu, V. Au, Z. Chen, Molybdenum phosphide coupled with highly dispersed nickel confined in porous carbon nanofibers for enhanced photocatalytic CO₂ reduction, *Chem. Eng. J.* 427 (2022), 131717.
- [7] F. You, J. Wan, J. Qi, D. Mao, N. Yang, Q. Zhang, L. Gu, D. Wang, Lattice distortion in hollow multi-shelled structures for efficient visible-light CO₂ reduction with a SnS₂/SnO₂ junction, *Angew. Chem. Int. Ed.* 59 (2020) 721–724.
- [8] Y. Li, M. Wen, Y. Wang, G. Tian, C. Wang, J. Zhao, Plasmonic hot electrons from oxygen vacancies for infrared light-driven catalytic CO₂ reduction on Bi₂O_{3-x}, *Angew. Chem. Int. Ed.* 60 (2021) 910–916.
- [9] L. Liang, F. Lei, S. Gao, Y. Sun, X. Jiao, J. Wu, S. Qamar, Y. Xie, Single unit cell bismuth tungstate layers realizing robust solar CO₂ reduction to methanol, *Angew. Chem. Int. Ed.* 54 (2015) 13971–13974.
- [10] N.E. Mendieta-Reyes, A.K. Díaz-García, R. Gómez, Simultaneous electrocatalytic CO₂ reduction and enhanced electrochromic effect at WO₃ nanostructured electrodes in acetonitrile, *ACS Catal.* 8 (2018) 1903–1912.
- [11] X. Jiao, X. Li, X. Jin, Y. Sun, J. Xu, L. Liang, H. Ju, J. Zhu, Y. Pan, W. Yan, Y. Lin, Y. Xie, Partially oxidized SnS₂ atomic layers achieving efficient visible-light-driven CO₂ reduction, *J. Am. Chem. Soc.* 139 (2017) 18044–18051.
- [12] S. Wang, B.Y. Guan, Y. Lu, X.W.D. Lou, Formation of hierarchical In₂S₃-CdIn₂S₄ heterostructured nanotubes for efficient and stable visible light CO₂ reduction, *J. Am. Chem. Soc.* 139 (2017) 17305–17308.
- [13] P. Chen, B. Lei, X. Dong, H. Wang, J. Sheng, W. Cui, J. Li, Y. Sun, Z. Wang, F. Dong, Rare-earth single-atom La-N charge-transfer bridge on carbon nitride for highly efficient and selective photocatalytic CO₂ reduction, *ACS Nano* 14 (2020) 15841–15852.
- [14] Z. Jiang, W. Wan, H. Li, S. Yuan, H. Zhao, P.K. Wong, A hierarchical Z-scheme alpha-Fe₂O₃/g-C₃N₄ hybrid for enhanced photocatalytic CO₂ reduction, *Adv. Mater.* 30 (10) (2018), 1706108, 30.
- [15] Y. Li, B. Li, D. Zhang, L. Cheng, Q. Xiang, Crystalline carbon nitride supported copper single atoms for photocatalytic CO₂ reduction with nearly 100% CO selectivity, *ACS Nano* 14 (2020) 10552–10561.
- [16] Z. Pan, E. Han, J. Zheng, J. Lu, X. Wang, Y. Yin, G.I.N. Waterhouse, X. Wang, P. Li, Highly efficient photoelectrocatalytic reduction of CO₂ to methanol by a p-n heterojunction CeO₂/CuO/Cu Catalyst, *Nano-Micro Lett.* 12 (2020) 18.
- [17] K.K. Ghuman, L.B. Hoch, P. Szymanski, J.Y. Loh, N.P. Kherani, M.A. El-Sayed, G. A. Ozin, C.V. Singh, Photoexcited surface frustrated Lewis pairs for heterogeneous photocatalytic CO₂ reduction, *J. Am. Chem. Soc.* 138 (2016) 1206–1214.
- [18] M.D. Porosoff, X. Yang, J.A. Boscoboinik, J.G. Chen, Molybdenum carbide as alternative catalysts to precious metals for highly selective reduction of CO₂ to CO, *Angew. Chem. Int. Ed.* 53 (2014) 6705–6709.
- [19] A. Call, M. Cibian, K. Yamamoto, T. Nakazono, K. Yamauchi, K. Sakai, Highly efficient and selective photocatalytic CO₂ reduction to CO in water by a cobalt porphyrin molecular catalyst, *ACS Catal.* 9 (2019) 4867–4874.
- [20] X. Li, Y. Sun, J. Xu, Y. Shao, J. Wu, X. Xu, Y. Pan, H. Ju, J. Zhu, Y. Xie, Selective visible-light-driven photocatalytic CO₂ reduction to CH₄ mediated by atomically thin CuIn₂S₄ layers, *Nat. Energy* 4 (2019) 690–699.
- [21] X. Zhang, Y. Liu, M. Zhang, T. Yu, B. Chen, Y. Xu, M. Crocker, X. Zhu, Y. Zhu, R. Wang, D. Xiao, M. Bi, D. Ma, C. Shi, Synergy between β-Mo₂C nanorods and non-thermal plasma for selective CO₂ reduction to CO, *Chem* 6 (2020) 3312–3328.
- [22] S.K. Kim, Y.J. Zhang, H. Bergstrom, R. Michalsky, A. Peterson, Understanding the low-overpotential production of CH₄ from CO₂ on Mo₂C catalysts, *ACS Catal.* 6 (2016) 2003–2013.
- [23] F. Calle-Vallejo, M.T. Koper, A.S. Bandarenka, Tailoring the catalytic activity of electrodes with monolayer amounts of foreign metals, *Chem. Soc. Rev.* 42 (2013) 5210–5230.
- [24] J. Di, C. Chen, S.Z. Yang, S. Chen, M. Duan, J. Xiong, C. Zhu, R. Long, W. Hao, Z. Chi, H. Chen, Y.X. Weng, J. Xia, L. Song, S. Li, H. Li, Z. Liu, Isolated single atom cobalt in Bi₂O₄Br atomic layers to trigger efficient CO₂ photoreduction, *Nat. Commun.* 10 (2019) 2840.
- [25] S. Zhao, S. Li, T. Guo, S. Zhang, J. Wang, Y. Wu, Y. Chen, Advances in Sn-based catalysts for electrochemical CO₂ reduction, *Nano-Micro Lett.* 11 (2019) 62.
- [26] Y. He, H. Rao, K. Song, J. Li, Y. Yu, Y. Lou, C. Li, Y. Han, Z. Shi, S. Feng, 3D hierarchical ZnIn₂S₄ nanosheets with rich Zn vacancies boosting photocatalytic CO₂ reduction, *Adv. Funct. Mater.* 29 (2019), 1905153.
- [27] S. Gong, X. Teng, Y. Niu, X. Liu, M. Xu, C. Xu, L. Ji, Z. Chen, Construction of S-scheme 0D/2D heterostructures for enhanced visible-light-driven CO₂ reduction, *Appl. Catal. B Environ.* 298 (2021), 120521.
- [28] M. Li, Y. Zhu, H. Wang, C. Wang, N. Pinna, X. Lu, Ni strongly coupled with Mo₂C encapsulated in nitrogen-doped carbon nanofibers as robust bifunctional catalyst for overall water splitting, *Adv. Energy Mater.* 9 (2019), 1803185.
- [29] A. Zhang, R. He, H. Li, Y. Chen, T. Kong, K. Li, H. Ju, J. Zhu, W. Zhu, J. Zeng, Nickel doping in atomically thin tin disulfide nanosheets enables highly efficient CO₂ reduction, *Angew. Chem. Int. Ed.* 57 (2018) 10954–10958.
- [30] H.B. Yu, J.H. Huang, L.B. Jiang, L.J. Leng, K.X. Yi, W. Zhang, C.Y. Zhang, X. Z. Yuan, In situ construction of Sn-doped structurally compatible heterojunction with enhanced interfacial electric field for photocatalytic pollutants removal and CO₂ reduction, *Appl. Catal. B Environ.* 298 (2021), 120618.
- [31] X. Teng, Y. Niu, S. Gong, M. Xu, X. Liu, L. Ji, Z. Chen, In/ZnO@C hollow nanocubes for efficient electrochemical reduction of CO₂ to formate and rechargeable Zn–CO₂ batteries, *Mater. Chem. Front.* 5 (2021) 6618–6627.
- [32] M. Tahir, N.S. Amin, Indium-doped TiO₂ nanoparticles for photocatalytic CO₂ reduction with H₂O vapors to CH₄, *Appl. Catal. B Environ.* 162 (2015) 98–109.
- [33] P.K. Santra, P.V. Kamat, Mn-doped quantum dot sensitized solar cells: a strategy to boost efficiency over 5%, *J. Am. Chem. Soc.* 134 (2012) 2508–2511.
- [34] S. Chen, H. Wang, Z. Kang, S. Jin, X. Zhang, X. Zheng, Z. Qi, J. Zhu, B. Pan, Y. Xie, Oxygen vacancy associated single-electron transfer for photofixation of CO₂ to long-chain chemicals, *Nat. Commun.* 10 (2019) 788.
- [35] W. Yang, Y. Zhao, S. Chen, W. Ren, X. Chen, C. Jia, Z. Su, Y. Wang, C. Zhao, Defective indium/indium oxide heterostructures for highly selective carbon dioxide electrocatalysis, *Inorg. Chem.* 59 (2020) 12437–12444.
- [36] J. Wu, X. Li, W. Shi, P. Ling, Y. Sun, X. Jiao, S. Gao, L. Liang, J. Xu, W. Yan, C. Wang, Y. Xie, Efficient visible-light-driven CO₂ reduction mediated by defect-engineered BiOBr atomic layers, *Angew. Chem. Int. Ed.* 57 (2018) 8719–8723.
- [37] S. Sorcar, Y. Hwang, C.A. Grimes, S.I. In, Highly enhanced and stable activity of defect-induced titania nanoparticles for solar light-driven CO₂ reduction into CH₄, *Mater. Today* 20 (2017) 507–515.
- [38] H. Shi, S. Long, S. Hu, J. Hou, W. Ni, C. Song, K. Li, G.G. Gurzadyan, X. Guo, Interfacial charge transfer in 0D/2D defect-rich heterostructures for efficient solar-driven CO₂ reduction, *Appl. Catal. B Environ.* 245 (2019) 760–769.
- [39] X. Zhang, Z. Chen, M. Jiao, X. Ma, K. Mou, F. Cheng, Z. Wang, X. Zhang, L. Liu, Defects and conductive nitrogen-carbon framework regulated ZnInOx nanosheets for boosting CO₂ electrocatalytic reduction, *Appl. Catal. B Environ.* 279 (2020), 119383.
- [40] W. Luc, C. Collins, S. Wang, H. Xin, K. He, Y. Kang, F. Jiao, Ag–Sn bimetallic catalyst with a core-shell structure for CO₂ reduction, *J. Am. Chem. Soc.* 139 (2017) 1885–1893.
- [41] Q. Li, J. Fu, W. Zhu, Z. Chen, B. Shen, L. Wu, Z. Xi, T. Wang, G. Lu, J.J. Zhu, S. Sun, Tuning Sn-catalysis for electrochemical reduction of CO₂ to CO via the core/shell Cu/SnO₂ structure, *J. Am. Chem. Soc.* 139 (2017) 4290–4293.

- [42] Z.C. Kong, J.F. Liao, Y.J. Dong, Y.F. Xu, H.Y. Chen, D.B. Kuang, C.Y. Su, Core@shell CsPbBr₃@zeolitic imidazolate framework nanocomposite for efficient photocatalytic CO₂ reduction, *ACS Energy Lett.* 3 (2018) 2656–2662.
- [43] L. Wang, J. Wan, Y. Zhao, N. Yang, D. Wang, Hollow multi-shelled structures of Co₃O₄ dodecahedron with unique crystal orientation for enhanced photocatalytic CO₂ reduction, *J. Am. Chem. Soc.* 141 (2019) 2238–2241.
- [44] X.F. Lu, Y. Chen, S. Wang, S. Gao, X.W.D. Lou, Interfacing manganese oxide and cobalt in porous graphitic carbon polyhedrons boosts oxygen electrocatalysis for Zn-air batteries, *Adv. Mater.* 31 (2019), 1902339.
- [45] X. Deng, Z. Wei, C. Cui, Q. Liu, C. Wang, J. Ma, Oxygen-deficient anatase TiO₂@C nanospindles with pseudocapacitive contribution for enhancing lithium storage, *J. Mater. Chem. A* 6 (2018) 4013–4022.
- [46] J. Liao, W. Cui, J. Li, J. Sheng, H. Wang, X. a Dong, P. Chen, G. Jiang, Z. Wang, F. Dong, Nitrogen defect structure and NO⁺ intermediate promoted photocatalytic NO removal on H₂ treated g-C₃N₄, *Chem. Eng. J.* 379 (2020), 122282.
- [47] J. Dong, Y. Lu, X. Tian, F.Q. Zhang, S. Chen, W. Yan, H.L. He, Y. Wang, Y.B. Zhang, Y. Qin, M. Sui, X.M. Zhang, X. Fan, Genuine active species generated from Fe₃N nanotube by synergistic CoNi doping for boosted oxygen evolution catalysis, *Small* 16 (2020), 2003824.
- [48] Y. Huang, Q. Gong, X. Song, K. Feng, K. Nie, F. Zhao, Y. Wang, M. Zeng, J. Zhong, Y. Li, Mo₂C nanoparticles ddispersed on hierarchical carbon microflowers for efficient electrocatalytic hydrogen evolution, *ACS Nano* 10 (2016) 11337–11343.
- [49] Y.L. Men, Y. You, Y.X. Pan, H. Gao, Y. Xia, D.G. Cheng, J. Song, D.X. Cui, N. Wu, Y. Li, S. Xin, J.B. Goodenough, Selective CO evolution from photoreduction of CO₂ on a metal-carbide-based composite catalyst, *J. Am. Chem. Soc.* 140 (2018) 13071–13077.
- [50] F. Devynck, A. Alkauskas, P. Broqvist, A. Pasquarello, Defect levels of carbon-related defects at the SiC/SiO₂ interface from hybrid functionals, *Phys. Rev. B* 83 (2011), 195319.
- [51] S. Sun, X. Zhou, B. Cong, W. Hong, G. Chen, Tailoring the d-band centers endows (Ni_xFe_{1-x})₂P nanosheets with efficient oxygen evolution catalysis, *ACS Catal.* 10 (2020) 9086–9097.
- [52] W. Zhong, R. Sa, L. Li, Y. He, L. Li, J. Bi, Z. Zhuang, Y. Yu, Z. Zou, A covalent organic framework bearing single Ni sites as a synergistic photocatalyst for selective photoreduction of CO₂ to CO, *J. Am. Chem. Soc.* 141 (2019) 7615–7621.